An improved upper limit to the CMB circular polarization at large angular scales

R. Mainini,^a D. Minelli,^{a,1} M. Gervasi,^a G. Boella,^a G. Sironi,^a A. Baú,^a S. Banfi,^a A. Passerini,^a A. De Lucia,^a F. Cavaliere^b

 ^aPhysics Department, University of Milano Bicocca, Milano, I20126
 ^bPhysics Department, University of Milano, Milano, I20133

E-mail: roberto.mainini@mib.infn.it

Abstract. Circular polarization of the Cosmic Microwave Background (CMB) offers the possibility of detecting rotations of the universe and magnetic fields in the primeval universe or in distant clusters of galaxies. We used the Milano Polarimeter (MIPOL) installed at the Testa Grigia Observatory, on the italian Alps, to improve the existing upper limits to the CMB circular polarization at large angular scales. We obtain 95% confidence level upper limits to the degree of the CMB circular polarization ranging between $5.0 \cdot 10^{-4}$ and $0.7 \cdot 10^{-4}$ at angular scales between 8° and 24°, improving by one order of magnitude preexisting upper limits at large angular scales. Our results are still far from the nK region where today expectations place the amplitude of the V Stokes parameter used to characterize circular polarization of the CMB but improve the preexisting limit at similar angular scales. Our observations offered also the opportunity of characterizing the atmospheric emission at 33 GHz at the Testa Grigia Observatory.

¹now at Institute of Plasma Physics of the Italian National Research Council, IFP-CNR, Milano

C	ontents	
O.	ontents	
1	Introduction	1
2	MIPOL : Milano Polarimeter	2
3	Observations	3
	3.1 Calibration and Tests	3
4	Data Reduction	6
	4.1 Total Power outputs	6
	4.2 Correlator outputs	8
5	Discussion	12
	5.1 Polarized component of the atmospheric signal	12
	5.2 Sky signal	12
6	Conclusion	16

1 Introduction

Polarization of the Cosmic Microwave Background (CMB) is a second order effect of matter radiation interactions during the Universe evolution. Linear polarization, produced by Thomson scattering of the CMB on matter anisotropies at the last scattering surface, has been detected at the μK level at various angular scales (e.g. [1–3]). Linear polarization can be produced also if CMB interacts with primordial gravitational waves. Detecting this component, known as B-modes of linear polarization and expected at the nK level or below, is extremely challenging. It is the aim of various experiments in preparation (e.g. [4, 5]).

The only attempts so far performed of detecting circular polarization of the CMB were made in the 80s when the search for fine structures of the CMB started (see Table 1). Circular polarization was in fact searched as a possible signature of non uniform expansion and rotation of the Universe which characterize some Bianchi Models [6–9]. The search however was abandoned when non uniform expansion and rotation of the Universe were not supported by other observations (e.g. [10]). But interest to constraining anisotropic expansion of the Universe is still present [11] and vorticities associated to Bianchi VII Cosmology have been strongly constrained but not completely excluded by the most recent CMB observations [12].

Other processes which may induce circular polarization of the CMB were then considered (e.g. [13, 14] and references therein). For instance circular polarization is expected beside linear polarization when the CMB Thomson scattering occurs in presence of background magnetic fields, (see [15] and references therein), or in weakly magnetized plasmas [16] and appears everytime the photon scattering is completely forward [17].

The expected amplitude of these circularly polarized signals is very faint, probably $\leq nK$, not very different from the expected amplitude of the B-modes linear polarization. But while experiments for detecting B-modes are currently underway no other experiment aimed at detecting circular polarization of the CMB at the same level or even at higher level has been proposed. The upper limits obtained by [18] and [19] (see Table 1) in the '80 are still the only results one can find in literature.

Reference	Wavelength	Angular scale	Polarization degree	Sky region
	$\lambda \text{ (cm)}$	$\Delta heta$	Π_V	
[18]	0.91	15°	$\leq 4 \cdot 10^{-3}$	$\delta = +37$
[19]	6.0	18'' - 160''	$\leq (2.2 - 0.6) \cdot 10^{-4}$	$\delta = +80$

Table 1. Summary of CMB circular polarization upper limits at 95% CL: $\Pi_V = V/T^{CMB}$.

In view of the information they can provide it seems now time for new attempts of detecting CMB circular polarization with sensitivities at nK level, but a few years will be necessary before they will be ready. So, while waiting for them we decided to exploit the almost unique capability of MIPOL, among the existing CMB instrumentation, and analyzed data we collected in 2009-2010.

2 MIPOL: Milano Polarimeter

Let's assume a radiation flux of brightness temperature T, mixture of polarized (temperature T_p) and unpolarized (temperature T_{up}) radiation. We can write $T_p = \sqrt{U^2 + Q^2 + V^2}$ where U, Q and V are the so called Stokes Parameters: U and Q describe the linearly polarized component of T_p , V the circularly polarized component, (see [20] and references therein).

MIPOL (Milano Polarimeter) is a 33 GHz ($\lambda = 9.1$ mm) two channel, $(0 - \pi)$ phase modulated, etherodyne correlation receiver [21], [22], [23]. From T MIPOL extracts a pair of Stokes Parameters of the radiation which hits the antenna: V and U (Circular or C-mode) or Q and U (Linear or L-mode). The antenna, a corrugated horn with an orthomode transducer, equipped with an apodized ground shield rigidly attached to the horn, has a 14° FWHM beam which can be reduced to 7° adding a proper extension to the horn mouth. The orthomode transducer splits the total (polarized and unpolarized) incoming radiation of temperature T in two linearly polarized components with crossed electric vectors \mathbf{E}_1 and \mathbf{E}_2 (temperatures $T_1 \propto E_1^2$ and $T_2 \propto E_2^2$) which then propagate through different channels Ch_1 and Ch_2 .

After proper amplification and coherent frequency conversion the two signals go to:

i) total power detectors whose outputs

$$TP_1 = S_{TP_1}T_1$$

 $TP_2 = S_{TP_2}T_2$ (2.1)

monitor the antenna temperatures T_1 and T_2 produced by polarized and unpolarized components of the sky signal plus system noise;

ii) a phase discriminator whose outputs

$$DT_{1} = S_{DT_{1}} \left[a \langle E_{1}E_{2} \rangle \cos(\gamma) + O_{1} \right] = S_{DT_{1}} \left[U \cos(\phi) - V \sin(\phi) + O'_{1} \right]$$

$$DT_{2} = S_{DT_{2}} \left[a \langle E_{1}E_{2} \rangle \sin(\gamma) + O_{2} \right] = S_{DT_{2}} \left[U \sin(\phi) + V \cos(\phi) + O'_{2} \right]$$
(2.2)

are linear combinations of the Stokes Parameters U and V (C-mode)of the polarized component of the incoming radiation.

In the above equations $\gamma = \theta + \phi$ is the sum of the phase difference ϕ introduced by the instrument and the intrinsic phase difference θ between \mathbf{E}_1 and \mathbf{E}_2 , S_{TPi} and S_{DTi} are

gain/conversion factors, O_i are post–processing offsets and offsets produced by circuit asymmetries and gain differences, not completely cancelled by phase modulation and synchronous detection (see [22] and [23]).

When a 90° iris polarizer is inserted between horn and orthomode transducer the antenna splits the signal in two components circularly polarized in opposite direction and DT_1 and DT_2 become linear combinations of U and Q (L-mode of operation).

After amplification, time integration ($\tau = 6s$) and analog to digital conversion (adc), TP_1 , TP_2 , DT_1 and DT_2 are sampled three times in a τ and stored. Each record is made of TP_1 , TP_2 , DT_1 , DT_2 , Giulian day, UT time, antenna pointing direction, environmental and housekeeping data.

MIPOL antenna and receiver are attached to a mechanical mount which allows to move the beam along the meridian and is driven by the same computer which stores the data.

MIPOL conceived at the beginning of the '90s to check the nature of the CMB anisotropies at large angular scales just detected by COBE-DMR [24], was prepared for observation from Antarctica, where prototypes were tested in 1994 at Terra Nova Bay [25] and in 1998 at Dome C - Concordia Station [26].

Because in the following years we did not have the opportunity for a new observation campaign from Antarctica, in 2002 we decided to install MIPOL on the Italian Alps at the Testa Grigia Observatory (lat=45.93 N, long=7.7 E, 3480 m asl). Here it was used as a test system of new polarization radiometers. Compared to more recently built ground and space experiments (e.g. PLANCK 1 , see [27]) it is no longer competitive with the exception of its capability of studying circular polarization. So we decided to exploit MIPOL C-mode and used data collected in 2009-2010 for improving the current upper limits of the CMB circular polarization.

3 Observations

Between Nov. 10th and Dec. 9th, 2009 we set MIPOL in C-mode, 7° beam, and performed drift scans of the sky while the beam moved back and forth along the meridian, at a constant pace between $\delta_{ini} = 41.1 \pm 0.1$ and $\delta_{fin} = 15.8 \pm 0.1$ in 300 s, then returned to δ_{ini} in 18 s. After a 48 s stop the cycle started again. Every 30 minutes the data stored on the PC hard disk were transferred via E-mail (smtp) to our Laboratory. Except for weekly checks the system run unattended. Weather conditions (cloud coverage, snow, wind), collected de visu when on site, or through a webcam when in Milano, were manually recorded on the log book.

Between Dec. 17th, 2009 and Jan. 20th, 2010 a small number of similar drift scans were made with MIPOL in L-mode. Insufficient to detect CMB linear polarization they were intended to verify MIPOL performance and to monitor the Testa Grigia environment conditions. Fig.1 shows the regions of sky covered by MIPOL during our campaign.

3.1 Calibration and Tests

The gain/conversion factors from digital units (adu) to temperature (K) (see eqs.(2.1) and (2.2)) were:

¹http://www.rssd.esa.int/index.php?project=planck

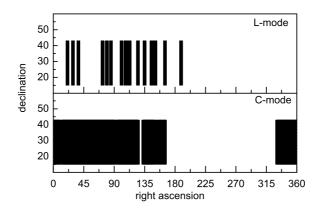


Figure 1. Bottom panel: Regions of sky observed in C-mode; Top panel: Regions of sky observed in L-mode.

- i) measured for TP_1 and TP_2 , coupling the antenna to an artificial blackbody source made of ECCOSORB[®] AN-72² set at different temperatures T_{bb} ranging between ambient temperature and liquid Nitrogren temperature.
- ii) calculated for DT_1 and DT_2 , propagating the measured total power values through the phase discriminator components whose gains and attenuations were carefully measured in laboratory. Offsets O_i (see eqs.(2.2)) can be obtained plotting DT_i vs T_{bb} . Different samples of data collected by MIPOL give values distributed around the average values shown in Table 2. Their values are related to the un-equalized electrical offset cancellation, while their dispersions reflect the very different environmental conditions occurred during the full data taking. A more accurate evaluation of the offsets has been performed using the fitting procedure described in Sec. 4.2, on the subsample used for the subsequent analysis. Results obtained on the subsample by the two methods coincide within the error bars. Accurate evaluation of the offset values are of importance only for measurements of the monopole term. But measuring it would require precise levels set by absolute sources of polarized radiation we do not have. For this reason in the following we will ignore the monopole term. On the other hand the residual fluctuations of the offset levels, which remain after the complete analysis described in Sec. 4.2, affects the accuracy of the determination we got on the Stokes parameters at the several angular scales.

Whenever necessary MIPOL behavior was checked using:

i) a (5×5) cm² flat grid of equally spaced parallel wires $(0.3 \text{ mm diameter}, \text{ spaced } 0.6 \text{ mm } << \lambda)$, which can be installed in the horn far field, parallel to the horn mouth, with its normal axis coincident with the horn axis. Crossed by the sky radiation, it injects in the horn a linearly polarized wave of temperature

$$T_p \simeq (\Omega_g/\Omega_h)[T_{sky}\sin^2(\theta_w) + T_{back}\cos^2(\theta_w)]$$
(3.1)

where T_{sky} is the sky temperature, Ω_g is the solid angle of the grid seen from the horn center of phase and Ω_h the solid angle of the horn beam $(\Omega_g/\Omega_h \sim 0.19)$, T_{back} is the noise back-reflected by the grid into the horn and θ_w is the angle respect to the wires direction. Rotating

²http://www.eccosorb.com/

	C-mode	L-mode	
Total Power			
S_{TP_1}	1165.8 ± 20.0	1220.3 ± 20.8	$\mathrm{adu/K}$
S_{TP_2}	1474.0 ± 25.4	1457.8 ± 23.9	$\mathrm{adu/K}$
$\Delta G_{TP1}/(\Delta t \ G_{TP1})$	$8.0 \ 10^{-9}$	$4.3 \ 10^{-9}$	s^{-1}
$\Delta G_{TP2}/(\Delta t \ G_{TP2})$	$6.4 \ 10^{-9}$	$4.4 \ 10^{-9}$	s^{-1}
Correlator			
S_{DT_1}	$(2.9 \pm 0.9) \cdot 10^5$	$(3.0 \pm 0.9) \cdot 10^5$	$\mathrm{adu/K}$
S_{DT_2}	$(2.9 \pm 0.9) \cdot 10^5$	$(3.0 \pm 0.9) \cdot 10^5$	$\mathrm{adu/K}$
O_1	$-(0.36 \pm 0.04) \cdot 10^5$	$(1.85 \pm 0.07) \cdot 10^5$	adu
O_2	$-(1.79 \pm 0.08) \cdot 10^5$	$-(1.06 \pm 0.06) \cdot 10^5$	adu
$\Delta G_{DT1}/(\Delta t \ G_{DT1})$	$4.3 \ 10^{-9}$	$4.0 \ 10^{-9}$	s^{-1}
$\Delta G_{DT2}/(\Delta t \ G_{DT2})$	$4.4 \ 10^{-9}$	$8.5 \ 10^{-9}$	s^{-1}

Table 2. MIPOL sensitivities, gain stabilities and correlator offsets.

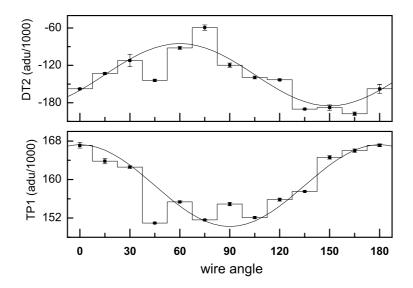


Figure 2. Modulation of MIPOL outputs produced by a rotating grid (see text) *Bottom panel*: Total Power TP_1 , C-mode. Top panel: Correlator DT_2 , C-mode. Histograms: observed modulation, with statistics error bars; smooth curve: trend of the expected ideal modulation (see eq. (3.1)).

the grid around its vertical axis we can modulate both total power (single mode and single polarized) channels and correlator outputs in a way which in principle is a simple sine law, proportional to the smooth curves shown in fig. 2. However grid back-reflection of the noise radiated by the horn and by the surrounding shield and horn mismatches produced by the grid itself and by grid supports make the effective modulations (histograms in fig. 2) more involved than that suggested by equation 3.1. In addition T_{back} is not easy to be estimated and, due to the not circularly symmetric grid support structure, should be dependent on θ_w . The grid signal therefore cannot be used for accurate calibrations. Grid modulation turns

out however very useful for checking that MIPOL remained sensitive to polarization: tiny quantities of dust or water vapor (produced by melting snow and ice needles) in the horn throat are in fact sufficient to make MIPOL deaf and completely cancel the dependence of TP_i and DT_i on the rotation angle. The grid signal depends on the environmental conditions, but it is well reproduced when similar conditions occur.

ii) a solid state noise generator³ which can be used to inject via directional couplers similar signals in both receiver channels ($T_1^{NG}=(3.17\pm0.04)$ K and $T_2^{NG}=(4.29\pm0.04)$ K in C-mode, $T_1^{NG}=(2.87\pm0.02)$ K and $T_2^{NG}=(3.42\pm0.03)$ K in L-mode). These signals, produced four times a day for 15 minutes, have been used to work out the gain stabilities of Mipol channels shown in Table 2.

4 Data Reduction

Only data collected at nighttime (i.e. between half an hour after sunset and half an hour before sunrise) have been analyzed. We then eliminated records which: i) contained anomalous housekeeping data, ii) showed odd values or odd variations of the receiver outputs, iii) were associated to bad weather conditions or to incomplete zenith scans. Here and in the following rejecting a value of DT_1 or DT_2 or TP_1 or TP_2 automatically causes rejection of the complete data record therefore of DT_1 and DT_2 and TP_1 and TP_2 and of all the records associated to the same zenith scan.

Right ascension α and declination δ of the beam axis were then calculated and added to each record. Records associated to tests and calibrations were separated and used to work out the system sensitivities S_{TP_i} and S_{DT_i} . Finally data were compressed in declination (δ) bins of 2° .

4.1 Total Power outputs

MIPOL does not include absolute references of temperature, therefore TP_1 and TP_2 have been used for monitoring environment conditions and MIPOL behavior, not for measurements of the CMB absolute temperature or anisotropy.

We expect:

$$\frac{TP_i}{S_{TP_i}}(\alpha, \delta, z) = T_i^{sky}(\alpha, \delta) + T_i^{atm}(z) + T_i^{gr}(z) + T_i^{rx}$$

$$\tag{4.1}$$

where

$$T_i^{sky}(\alpha, \delta) = T_i^{CMB} + T_i^{gal}(\alpha, \delta) + T_i^{ex}$$

$$\tag{4.2}$$

Here, z is the beam zenith angle, $T_i^{CMB}, T_i^{gal}(\alpha, \delta)$ and T_i^{ex} the brightness temperature of CMB, Galactic emission and blend of unresolved extragalactic sources, respectively. $T_i^{atm}(z)$ and T_i^{rx} are the atmosheric signal and the receiver noise while $T_i^{gr}(z) = T_{i,min}^{gr} + \Delta T_i^{gr}(z)$ is the contribution of ground and other undesired emission from the environment, which overcome the antenna ground screen. Because of obstacles northward of MIPOL axis, $T_i^{gr}(z)$ was minimum when z is close to 0, not exactly at z=0. At 33 GHz and MIPOL angular

³Hewlett-Packard HP R347B

resolution we expect $T^{gal} \lesssim 4$ mK [28, 29], $T^{ex} \approx 15 \mu$ K [30] and $\Delta T_i^{gr}(z) \ll T_i^{atm}(z)$ so to first approximation:

$$\frac{TP_i}{S_{TP_i}} \simeq T_i^{CMB} + T_i^{atm}(z) + T_i^{sys} \tag{4.3}$$

where $T_i^{sys} = T_i^{rx} + T_{i,min}^{gr}$ is the system noise.

Total power analysis was carried out for the full samples of C- and L-mode data, and then repeated for the subsample of C-mode data on which the correlator analysis was performed (see Section 4.2 for details).

The Time Ordered Data (TOD) restricted to the subsample are displayed in Fig. 3 for both TP_i and DT_i . The same set of data is then used in all the subsequent plots where, at difference from Fig. 3, the mean values of the zenith scans have been equalized to their average value.

For each sample, the atmospheric noise temperature T_i^{atm} has been extracted from the zenith scans fitting them with a secant law $T_i^{atm}(z) = T_i^{atm} f(z)$ where $f(z) = \sec(z) * \mathcal{G}$ is the convolution of $\sec(z)$ over the antenna beam \mathcal{G} (which is assumed to be Gaussian).

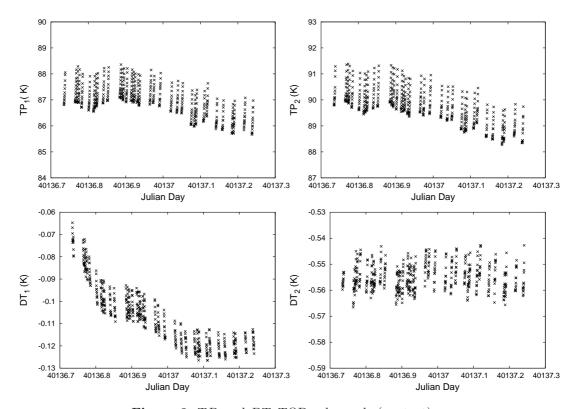


Figure 3. TP_i and DT_i TOD subsample (see text).

The resulting values are consistent with model expectations [31] and summarized in Table 3. C-mode fits are shown in Fig. 4.

Differences between the atmospheric temperatures extracted from the full samples of data obtained while MIPOL was in C- and L-mode are consistent with variability of weather conditions: frequent perturbations and higher nighttime temperatures ($< T_{env} >= -9.3 \pm 4.0$ C) in November - beginning December 2009, clear sky, stable weather conditions and colder nights ($< T_{env} >= -17.2 \pm 5.6$ C), at the end of December 2009 and in January 2010.

	L-mode	C-mode	C-mode	
	full sample	full sample	subsample	
T_1^{atm}	9.55 ± 0.21	7.91 ± 0.04	8.45 ± 0.04	K
T_2^{atm}	7.25 ± 0.26	8.70 ± 0.05	9.49 ± 0.06	K
T_1^{sys}	83.6 ± 1.4	82.9 ± 1.4	75.36 ± 0.05	K
T_2^{sys}	89.7 ± 1.5	84.1 ± 1.5	76.05 ± 0.07	K

Table 3. Atmospheric and system temperatures from Total Power measurements. Results are reported for the full sample of data (both for C-mode and L-mode) and the C-mode subsample described in the text.

More noticeable are the differences between the C-mode results obtained from the full sample and the subsample. They reflect the large variability of observing and system conditions during the entire period of observations compared to the stable conditions, which produced uniform sky coverage, during the night when the entire subsample was collected (see next Section).

Subtractions of the atmospheric signals from TP_i zenith scans leaves a residual z dependence produced by the increasing fraction of ground emission which overcomes the ground screen as the antenna moves along the meridian toward the horizon. After subtraction of atmospheric signal and ground excess $\Delta T_i^{gr}(z)$, $TP_1(\alpha, \delta)$ and $TP_2(\alpha, \delta)$ become z independent. Removing $T^{CMB} = 2.018$ K, the brightness temperature of the CMB at 33 GHz, gives the system noise T_i^{sys} (see Table 3).

4.2 Correlator outputs

Because of the limited quantity of L-mode data and our interest for circular polarization, here and in the following only C-mode data have been used.

Shapes of the correlator zenith scans are poorly defined and depend on weather conditions. Moreover their base levels vary day by day because of: i) slow variations of gain and system noise (not evident on TP_i profiles because of the very different sensitivities of correlator and total power (see Table 2)); ii) polarization by reflection of ground contribution (see section 4.1) and dependence of the ground reflectivity on the humidity.

The set of C- mode correlator data can be divided in two groups: i) a subsample of data collected in the night between Julian days 40136 and 40137, when the observing conditions were particularly good. Characterized by rms fluctuations of DT_1 and DT_2 equal to $\sigma_1 \simeq 0.7~mK$ and $\sigma_2 \simeq 0.9~mK$ respectively, the data of this subsample fill uniformly the region of sky observed by MIPOL, show a uniform distribution respect to elevation and time, and represent 1/3 of the complete sample of C-mode data; ii) the remaining data characterized by $\sigma_1 \simeq 1.8~mK$ and $\sigma_2 \simeq 1.9~mK$. They are definitely more noisy, their distribution on the sky is irregular and were collected when the observing conditions were definitely worse. Combining the two sets of data the statistics increases but fluctuations are $\sigma_1 \simeq 1.5~mK$ and $\sigma_2 \simeq 1.6~mK$, definitely worse than the subsample values. We decided therefore to concentrate our analysis using the smaller but cleaner subsample only.

$\tan(\gamma_{atm})$	$T_{corr}^{atm,0}$ (K)	$\tan(\gamma_{gr})$	$T_{corr}^{gr,0}$ (K)
-1.68 ± 0.09	0.087 ± 0.002	-0.24 ± 0.06	0.006 ± 0.046

Table 4. Correlator phase differences γ_X (see text) and estimated atmospheric and ground polarized emissions.

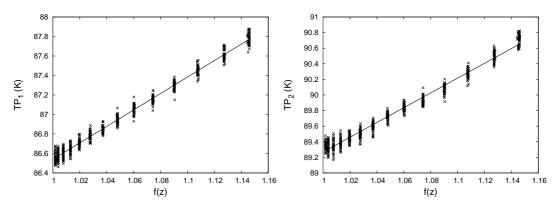


Figure 4. Total Power zenith scan profiles TP_i . Data are compressed in declination bins of 2° and plotted versus $f(z) = \sec(z) * \mathcal{G}$, the convolution of $\sec(z)$ over the antenna beam \mathcal{G} . Data are well fitted by a secant law (solid lines).

Let us rewrite eq. (2.2) emphasizing the contribution of the different sources:

$$\frac{DTi}{S_{DTi}}(z) = \frac{1}{S_{DTi}} \sum_{X} DT_i^X$$

$$= a \sum_{X} \langle E_1^X E_2^X \rangle h_i(\gamma_X) + O_i \tag{4.4}$$

where we made use of the correlation properties of radiation $(\langle E_1^X E_2^Y \rangle = 0 \text{ for } X \neq Y)$ and set $h_1(\gamma_X) = \cos(\gamma_X)$, $h_2(\gamma_X) = \sin(\gamma_X)$ and $\gamma_X = \theta_X + \phi$

Marking the z dependence we can write:

$$\frac{DTi}{S_{DTi}}(z) = a\left[\left\langle E_1^{atm} E_2^{atm} \right\rangle_0 f^c(z) h_i(\gamma_{atm}) + \left\langle E_1^{gr} E_2^{gr} \right\rangle_0 g^c(z) h_i(\gamma_{gr})\right] + O_i \tag{4.5}$$

where: i) $\langle \ \rangle_0$ marks correlated signals at z=0; ii) no receiver noise correlation term is present because the noises in channel 1 and 2 are generated independently; iii) the sky signal, dominated by CMB, has a negligible z dependence; iv) the z dependences of atmospheric and ground signals are described by $f^c(z)$ and $g^c(z)$ respectively.

Setting $f^c(z) = \sec(z) * \mathcal{G}$, we can fit the DT_i zenith scan profiles adding a term of order 8 in $f^c(z)$, which accounts for $g^c(z)$, (see Fig. 5). We get

$$DT_i(f^c(z)) = d_{0,i} + d_{1,i}f^c(z) + d_{8,i}(f^c(z) - 1.146)^8$$
(4.6)

Comparing eqs. (4.6) and (4.5), the coefficients $d_{1,i}$ and $d_{0,i}$ of the linear term (see Fig. 5)

$$DT_i^{lin}(f^c(z)) = d_{0,i} + d_{1,i}f^c(z)$$
(4.7)

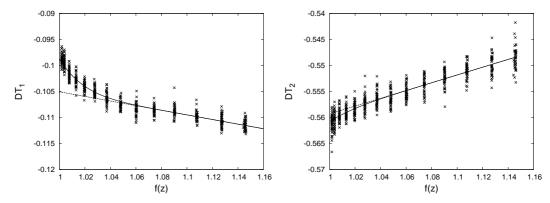


Figure 5. Same as in Fig. 4 but for the correlator zenith scan profiles DT_i . Deviations from a pure secant law (dashed lines) at small zenith angles are here evident due to ground contaminations and unknown environmental effects. Data at small angles are well fitted by polinomyals of order 8 in f(z) (solid lines).

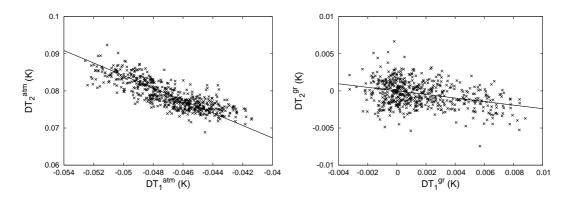


Figure 6. DT_2 versus DT_1 plots for atmospheric (*left*) and ground (*right*) signals. The angular coefficients of the fits (solid lines) give the phase differences γ_{atm} and γ_{gr} (see text).

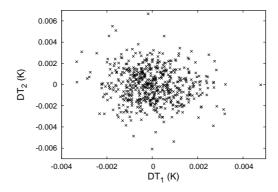


Figure 7. DT_2 versus DT_1 plot after removing atmospheric and ground emissions and offsets (see text).

pixel size	pixels	$\langle V \rangle$	σ_V	σ_V^{pix}	$\sigma^{pix}_{\langle V \rangle}$	
$2^{\circ} \times 2^{\circ}$						
unbinned data	518	-0.02 ± 0.06	1.29			mK
$8^{\circ} \times 8^{\circ}$	64	-0.02 ± 0.08	0.64	1.14	0.43	mK
$12^{\circ} \times 12^{\circ}$	32	-0.02 ± 0.07	0.38	1.27	0.35	mK
$24^{\circ} \times 24^{\circ}$	9	-0.02 ± 0.06	0.15	1.37	0.21	mK

Table 5. CMB Stokes Parameter V from an unbinned map, dominated by the system noise, insensitive to sky signal (upper section) and three maps at different angular resolutions sensitive to sky signal (lower section). The Table columns show: pixel size, number of pixels, mean $\langle V \rangle$, standard deviation σ_V over the full maps, average rms per pixel σ_V^{pix} and average standard deviation of the mean per pixel $\sigma_{\langle V \rangle}^{pix}$.

can be identified with $\langle E_1^{atm} E_2^{atm} \rangle_0 h_i(\gamma_{atm})$ and O_i respectively. The resulting values of O_i ($O_1 = -(0.177 \pm 0.006) \cdot 10^5 adu = -(0.061 \pm 0.002)K$, $O_2 = -(1.839 \pm 0.009) \cdot 10^5 adu = -(0.634 \pm 0.003)K$)). Only the monopole term, we will not consider here, depends on these values. The fluctuation of O_i , after removing the residual linear dependence with the environment temperature, described later in the present section, set the final accuracy on the Stokes parameters at the several angular scales. The last term in eq. (4.6), which describes deviations from the secant law, accounts for ground excess $\langle E_1^{gr} E_2^{gr} \rangle_0 g^c(z) h_i(\gamma_{gr})$ and other unknown contributions.

 $\langle E_1^{gr}E_2^{gr}\rangle_0 g^c(z)h_i(\gamma_{gr})$ and other unknown contributions. We can now obtain the phase differences $\gamma_{atm}=\tan^{-1}\left(d_{1,2}/d_{1,1}\right)$ and $\gamma_{gr}=\tan^{-1}\left(d_{8,2}/d_{8,1}\right)$: they are the angular coefficients of the lines shown in Fig. 6 (alternatively they can be obtained plotting DT_2^X versus DT_1^X). Finally we get the correlated (therefore polarized) components of the atmospheric $T_{corr}^{atm,0} \propto \langle E_1^{atm}E_2^{atm}\rangle_0$ and ground $T_{corr}^{gr,0} \propto \langle E_1^{gr}E_2^{gr}\rangle_0$ emissions (see the next Section for a discussion on the atmospheric signal).

After removing them and offsets, and correcting for a residual linear dependence of the resulting time profiles of DT_i at constant z on the environment temperature, no significant correlation is observed between DT_1 and DT_2 (correlation coefficient $\rho = -0.09$, see Fig 7) indicating the polarized signal is completely buried in the instrumental noise.

Furthermore, the expected degree of polarization of the atmospheric emission, if present, must be very low so that the signal can be supposed unpolarized and we can assume $\theta_{atm} << \phi$. It follows $\gamma_{atm} \simeq \phi$ and $\gamma_{gr} = \theta_{gr} + \phi$. The resulting values of $T_{corr}^{X,0}$ and γ_X (X = atm, gr) are summarized in Table 4 together with the $1 - \sigma$ uncertainties.

We can therefore work out the sky Stokes parameters U and V inverting:

$$DT_1 \propto U \cos(\phi) - V \sin(\phi)$$

$$DT_2 \propto U \sin(\phi) + V \cos(\phi)$$
(4.8)

The resulting Stokes parameters U and V of the sky signal were finally arranged in squared bins to form maps with resolution $2^{\circ}, 8^{\circ}, 12^{\circ}$ and 24° . The maps are noise dominated and do not show statistically significant features.

Concentrating our attention on V circular polarization Stokes parameter for each V map we calculated (Table 5): i) V mean value $\langle V \rangle$ (with $1-\sigma$ uncertainty); ii) standard deviation σ_V calculated over the full map; iii) average value of the rms per pixel σ_V^{pix} ; iv) average standard deviation of the mean per pixel $\sigma_{\langle V \rangle}^{pix}$; v) $\langle V \rangle$ and σ_V for the un-binned data.

Because the bins of the $2^{\circ} \times 2^{\circ}$ map are smaller than MIPOL angular resolution, at this angular scale the sky signal is washed out and the system noise dominates. Therefore in the following the V and σ values of the $2^{\circ} \times 2^{\circ}$ map will be marked V_{noise} and σ_{noise} . For the map at 8° , 12° and 24° the V and σ , combinations of noise and sky signal, will be marked V_{obs} and σ_{obs} .

5 Discussion

5.1 Polarized component of the atmospheric signal

Circular polarization of the atmospheric emission is produced by Zeeman effect on the oxygen molecules therefore depends on the angle ϵ between the line of sight and the geomagnetic field line at the site of observation ⁴. Following [32]: i) $f_{O_2}^c = \sec(z)\cos(\epsilon)$; ii) at the Testa Grigia Observatory (lat=45.93 N, long=7.7 E) the Earth magnetic field line is approximately on the meridian plane, points northward and the angle between field line and zenith direction is $\epsilon_0 \simeq 151.9$ deg; iii) at MIPOL operating frequency (33 GHz) we can expect $V_{O_2}^{33GHz} \sim 50-70~\mu K$ at z=0 with an increase ($\Delta V \sim 15-25~\mu K$) looking z=30 deg southward. So we can write $\epsilon \simeq z + \epsilon_0$ and $f_{O_2}^c(z) = \sec(z)\cos(z+\epsilon_0)$.

Fitting our zenith scan profiles of DT_1 and DT_2 assuming $f^c(z) \simeq f_{O_2}^c(z)$ we obtain results compatible with the results previously obtained assuming $f^c(z) = \sec(z)$. Differences between the two fitting functions are in fact small. The differences become important close to z = 0, where the increase of the ground contribution produced by northward obstacles makes this analysis unreliable. Last but not least the signal we obtain is too large and cannot be associated to polarized emission of the atmospheric oxygen. We are rather lead to ascribe the signal correlated to the scans to $I \to (V, U)$ contamination of the correlator outputs by the much stronger unpolarized atmospheric signal measured in total power.

Therefore $T_{corr}^{atm,0}$ is an upper limit to the circularly polarized emission of the atmospheric oxygen and we can write $V_{O_2}^{33GHz}(z=0) < 87$ mK and quantify the $I \to (V,U)$ contamination by

$$\Gamma(I \to V, U) = \frac{T_{corr}^{atm,0}}{\sqrt{T_1^{atm,0} T_2^{atm,0}}} = 9.7 \times 10^{-3}$$
 (5.1)

5.2 Sky signal

The monopole term of V and the very large scale fluctuations approximately constant over the map size are hidden in the large instrumental offsets and can not be discriminated with our measurement apparatus. Removing offsets then makes the average values of V, in our maps consistent with zero at the angular scales we considered (see Table 5).

Upper limits on the degree of the CMB circular polarization are obtained with three different methods (see below) which rely on the assumption that data are drawn from a Gaussian distribution. In order to check the validity of this assumption, we perform a χ^2 test for the distributions of the measured V values at angular scales of 2° , 8° and 12° . Because of the small number of independent pixels, χ^2 test is meaningless at 24° resolution. For each scale, we assume a Gaussian model with mean μ and standard deviation σ estimated from:

i) data, assuming $\mu = \langle V \rangle$ and $\sigma = \sigma_V$ (see Table 5) or, alternatively, best-fitting the observed distibutions;

 $^{^4}http://omniweb.gsfc.nasa.gov/vitmo/cgm_vitmo.html$

pixel size	£	$\mu = \langle V \rangle \ \sigma = \sigma_V$		best-fit		simulations	
pixer size	J	χ^2	P	χ^2	P	χ^2	P
$8^{\circ} \times 8^{\circ}$	5	6.04	0.70	3.90	0.44	9.95	0.92
$12^{\circ} \times 12^{\circ}$	1	1.96	0.76	0.79	0.55	2.81	0.83
$2^{\circ} \times 2^{\circ}$	55		$\chi^2 = 46.60 P = 0.20$				

Table 6. χ^2 test for assessing the Gaussianity of the data. We list the number of degree of freedom f, χ^2 , and the corresponding probability P of the assumed Gaussian model. See the text for details.

ii) Monte Carlo simulations. We generate 10000 random Gaussian realizations of our $2^{\circ} \times 2^{\circ}$ map (same number of data, mean and variance), and then bin at 8° and 12° . Model parameters μ and σ are evaluated from the distributions of the simulated data at the angular scales considered.

In Table 6 we list the number of degree of freedom f, χ^2 , and the corresponding probability P of the assumed Gaussian model. At 2°, the distribution of the data is Gaussian to a very good approximation. Al larger angular scales, we can claim that data are consistent, at 95% C.L., with the hypothesis of Gaussianity.

All the circularly polarized signals, both those of astrophysical origin (Galactic synchrotron, blend of unresolved extragalactic sources, SZ effect), and those of cosmological origin, associated to the CMB, are expected at the μK level or below. Therefore all the sky signals at 8°, 12° and 24° are completely buried in the MIPOL noise and the rms per pixel, σ_V^{pix} , is consistent with the fluctuations σ_V of the unbinned (2° × 2°) data. For each map we also expect $\sigma_V \simeq \sigma_{\langle V \rangle}^{pix}$. Slight deviations found at 8° and 24° scales reflect the limited statistics of those maps (few measurements per pixel at 8° resolution, small number of pixels at 24°).

For each of the above components of the sky signal and their sum (no component stands up above the others) we use three different approaches in order to set 95% upper limits at the angular scales of 8°, 12° and 24°:

Method I - We can write:

$$\sigma_{obs}^2(\theta) = \sigma_{sky}^2(\theta) + \sigma_{noise}^2(2^{\circ} \times 2^{\circ})/(\theta/2^{\circ})^2 \tag{5.2}$$

where $\sigma_{noise}(2^{\circ} \times 2^{\circ}) = 1.29$, $\sigma_{obs} = \sigma_{V}$ (see Table 5), and get $\sigma_{sky}(\theta)$. The resulting upper limits (at 95% CL) to the degree of circular polarization of CMB, $\Pi_{V}^{CMB} = w/T^{CMB}$, (w is the width of the probability distribution at 95% and in this case $w = 2\sigma_{sky}$) are shown in Table 7.

Method II - A Bayesian approach [19] allows a different estimate. We can write

$$P(\sigma_{sky}|\{V_i\}) = \mathcal{N} \ p(\sigma_{sky}) \ P(\{V_i\}|\sigma_{sky}) \tag{5.3}$$

where $P(\sigma_{sky}|\{V_i\})$ is the probability that σ_{sky} is consistent with the observed distribution $\{V_i\} = V_{obs}$,

$$P(V_i|\sigma_{sky}) = \prod_i \frac{1}{\left[2\pi(\sigma_i^2 + \sigma_{sky}^2)\right]^{\frac{1}{2}}} e^{-\frac{1}{2}\frac{V_i^2}{\sigma_i^2 + \sigma_{sky}^2}}$$
(5.4)

is the likelihood distribution of the measurements (σ_i is the standard deviation of the i^{th} measurement), $p(\sigma_{sky})$ the probability density of σ_{sky} assumed flat (uniform prior) and \mathcal{N} a

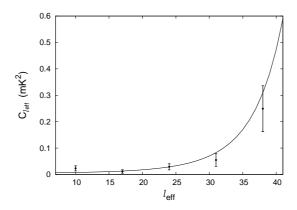


Figure 8. Binned angular power spectrum $C_{l_{eff}}$ from data (signal plus noise) compared to the expected power spectrum (solid line) for pure Gaussian noise.

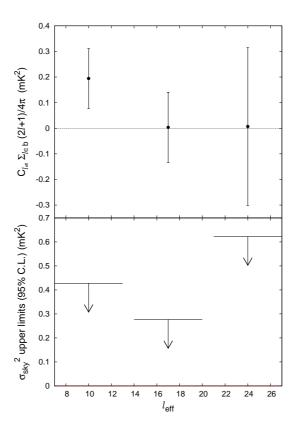


Figure 9. Top panel: Angular power spectrum of V-mode polarization fluctuations; Bottom panel: 95% C.L. upper limits.

normalization constant. The values of σ_{sky} above which lay less than 5% of the probability curve, reported in Table 7, represent the upper limits (at 95% CL) for the circular polarization degree.

Method III - Spherical harmonics analysis - Finally, we apply the maximum like-

method	I		II
pixel size		Π_V^{CMB}	
$8^{\circ} \times 8^{\circ}$	$5.0 \cdot 10^{-4}$		$4.0 \cdot 10^{-4}$
$12^{\circ} \times 12^{\circ}$	$2.7 \cdot 10^{-4}$		$3.2 \cdot 10^{-4}$
$24^{\circ} \times 24^{\circ}$	$0.7 \cdot 10^{-4}$		$2.1 \cdot 10^{-4}$

Table 7. Upper limits to the degree of circular polarization of the CMB calculated by classical methods and bayesian methods (see the text).

method II	method III - spherical harmonics analysis				
Δl	$<\theta>$	Π_V^{CMB}			
7 - 13	18.0°	$2.7 \cdot 10^{-4}$			
14 - 20	10.6°	$2.4 \cdot 10^{-4}$			
21 - 27	7.5°	$4.3 \cdot 10^{-4}$			

Table 8. Upper limits to the degree of circular polarization of the CMB calculated by spherical harmonics analysis methods (see the text).

lihood method described in [33] to estimate the angular power spectrum C_l of V-mode polarization. The method is a trivial application of Bayes' theorem and assume that fluctuations in both sky signal and experimental noise are Gaussian. C_l 's are estimated with a quadratic estimator which can be derived from a Gaussian approximation to the likelihood function:

$$\mathcal{L}(C_l) = P(V_i|C_l) = \frac{1}{\left[2\pi^{N_{pix}} \det C\right]^{1/2}} e^{-\frac{1}{2}V_i C_{ij}^{-1} V_j}$$
(5.5)

where N_{pix} is the number of pixels in the map and the total covariance matrix $C_{ij} = S_{ij}(C_l) + N_{ij}$ is the sum of the theoretical signal covariance matrix S_{ij} , which depends on the pameters to be estimated, and the instrumental noise covariance matrix N_{ij} estimated from data (assuming uncorrelated and Gaussian noise).

The Gaussian approximation is equivalent to truncating the Taylor series expansion of $\ln \mathcal{L}(C_l + \delta C_l)$ to second order term. This allows to solve iteratively for C_l 's that maximize $\mathcal{L}(C_l)$ starting from an initial guess C_l^0 :

$$C_l^{i+1} = C_l^i + \delta C_l$$

with

$$\delta C_{l} = \frac{1}{2} \sum_{l'} F_{ll'}^{-1} \frac{\partial \ln \mathcal{L}}{\partial C_{l'}}$$

where $F_{ll'}$ is the C_l 's Fisher matrix.

Given the limited extent of our map, features in the power spectrum will be smeared out on scale smaller than $l \sim \pi/\theta$, (θ is the size of the observed region in the narrowest direction), making multipoles on those scale strongly correlated [34]. Thus, we binned multipoles in bins of width $\Delta l = 7 \simeq \pi/\theta$. The signal covariance matrix then reads:

$$S_{ij} = \sum_{b} C_{l_{eff}} \sum_{l \in b} \frac{2l+1}{4\pi} W_l P_l(\cos \theta_{ij})$$

where we have assumed that the power spectrum is constant in each l-band b. The sum over l extends across the bin b, $C_{l_{eff}}$ is the binned power spectrum and l_{eff} indicates the central value of the bands. $P_l(\cos\theta_{ij})$ are the Legendre polinomials and θ_{ij} is the angular separation between pixels i and j. W_l is the beam window function.

In order to have equal area pixels in our map, we use the icosahedron-based pixelization method proposed in [35] setting the pixel size to $\sim 4^{\circ} \times 4^{\circ}$.

Fig. 8 shows the binned angular power spectrum $C_{l_{eff}}$ of our data (signal plus noise) compared to the expected power spectrum (solid line) for pure Gaussian noise $N_l = \sigma_{pix}^2 \Omega_{pix}/W_l$ with pixel variance σ_{pix}^2 and area Ω_{pix} equal to the variance and pixel area of our map. The $1-\sigma$ error bar are derived from the Fisher matrix. Data and theoretical noise spectra agree at $\sim 1-\sigma$ level confirming that all the circularly polarized signals are well buried in the noise and the validity of the Gaussian statistic up to the largest angular scales we observed.

The upper panel of Fig. 9 displays the binned power spectrun of the signal obtained from the maximum likelihooh method with $1-\sigma$ Fisher matrix error bars. The values on the abscissa are $C_{l_{eff}} \sum_{l \in b} \frac{2l+1}{4\pi}$ which correspond to the mean variance σ_{sky}^2 in the l-band b. The 95% C.L. upper limits on σ_{sky}^2 are shown in the bottom panel of Fig. 9 (horizontal lines donote the bin width) while the polarization degrees in each band are summarized in Table 8. Results are given for angular scale larger than the beam width ($l \lesssim 30$), higher multipoles being suppressed by the beam window function. Further, due to the limited size of the map, lowest multipole ($\Delta l = 1-6$) can not be accurately determinated and are disregarded.

6 Conclusion

We obtain 95% CL upper limits to the degree of the CMB circular polarization ranging between $5.0 \cdot 10^{-4}$ and $0.7 \cdot 10^{-4}$ at angular scales between 8° and 24°. Results obtained with three different methods are consistent each other. Our observations improve the pre-existing upper limits to the CMB circular polarization at large angular scales by an order of magnitude. However they are still very far from the nK region where probably V^{CMB} lays. Therefore they cannot be reasonably used to set significant upper limits to primordial magnetic field or rotation of the Universe.

We point out however once more that detecting CMB circular polarization offers the possibility of detecting important features of the primeval Universe and magnetic fields in distant clusters today studied by the SZ effect [36]. The expected signal is possibly not fainter than the amplitude of the B-mode linear polarization that various CMB experiments are looking for. It is therefore highly desirable that the new generations of CMB experiments will include the possibility of looking for circular polarization.

Acknowledgments

We are grateful to the referee for helpful comments that have improved the manuscript. MIPOL activity has been supported by MIUR (Italian Ministry of University and Research), CNR (Italian Research National Council) the Universities of Milano and of Milano-Bicocca and the Italian Antarctic Program (PNRA). We thanks our colleagues of Istituto of Cosmogeofisica of CNR-Turin for hosting us and our systems at Testa Grigia Observatory and students E. Boera, D. Colombo, S. Cotini, L. Di Gesú, V.Galardo, C. Taparello, who helped us to keep the system running at Testa Grigia in winter 2009-2010. L. Colombo is also thanked for useful discussions and suggestions.

References

- [1] J. Kovac et al., Detection of polarization in the cosmic microwave background using DASI, Nature 420 (2002) 772, astro-ph/0209478
- [2] WMAP collaboration, A. Kogut et al., Wilkinson Microwave Anisotropy Probe (WMAP) first year observations: TE polarization, Astrophys. J. Suppl. 148 (2003) 161, astro-ph/0302213
- [3] T.E. Montroy et al., A Measurement of the CNB < EE > spectrum from the 2003 flight of BOOMERANG, Astrophys. J. 647 (2006) 813, astro-ph/0507514
- [4] QUBIC collaboration, E. Battistelli et al., QUBIC: The QU Bolometric Interferometer for Cosmology, Astropart. Phys. 34 (2011) 705, arXiv:1010.0645
- [5] LSPE collaboration, S. Aiola et al., The Large-Scale Polarization Explorer (LSPE), arXiv:1208.0281
- [6] J. Negroponte and J. Silk, Polarization of the primeval radiation in an anisotropic universe, Phys. Rev. Lett. 44 (1980) 1433
- [7] M.M Basko and A.G. Polnarev, Polarization and anisotropy of the RELICT radiation in an anisotropic universe, Mon. Not. Roy. Astron. Soc. 191 (1980) 207
- [8] R. Stark, The radiative polarization transfer equations in hot Comptonizing electron scattering atmospheres including induced scattering, Mon. Not. Roy. Astron. Soc. 195 (1981) 115
- [9] B.W. Tolman and R.A. Metzner, Large scale anisotropies and polarization of the microwave background radiation in homogeneous cosmologies, Proc. Roy. Soc. London A 392 (1984) 391.
- [10] Supernova Cosmology Project collaboration, S. Perlmutter et al., Measurements of Omega and Lambda from 42 high redshift supernovae, Astrophys. J. 517 (1999) 565, astro-ph/9812133
- [11] R.G. Cai, Y.-Z. Ma, B. Tang and Z.-L. Tuo, Constraining the Anisotropic Expansion of Universe, Phys. Rev. D 87, 123522 (2013), arXiv:1303.0961
- [12] Planck collaboration, P. Ade et al., Planck 2013 results. XXVI. Background geometry and topology of the Universe, arXiv:1303.5086
- [13] A. Cooray, A. Melchiorri and J. Silk, Is the cosmic microwave background circularly polarized?, Phys. Lett. B 554 (2003) 1, astro-ph/0205214
- [14] E. Bavarsad, M. Haghighat, Z. Rezaei, R. Mohammadi, I. Motie and M. Zarei, Generation of circular polarization of the CMB, Phys. Rev. D 81 (2010) 14, arXiv:0912.2993
- [15] M. Giovannini, A Circular Polarimeter for the Cosmic Microwave Background, JCAP 08 (2010) 028, arXiv:1003.5892
- [16] M. Giovannini, Cosmic microwave background polarization, Faraday rotation and stochastic gravity-waves backgrounds, Phys. Rev. D 56 (1997) 3198, hep-th/9706201
- [17] R. Sawyer, Photon-photon interactions as a source of CMB circular polarization, arXiv:1205.4969
- [18] P.M. Lubin, P. Melese and G.F. Smooth, Linear and circular polarization of the cosmic background radiation, Astrophys. J. 273 (1983) L51.
- [19] R.B Partridge et al., Linear polarized fluctuations in the cosmic microwave background, Nature 331 (1988) 146
- [20] J.D. Krauss, Radio Astronomy, Mc Graw Hill, New York (1966)
- [21] G. Sironi et al., A 33 GHz polarimeter for observations of the Cosmic Microwave Background, New Astron. 3 (1998) 1

- [22] D. Spiga, E. Battistelli, G. Boella, M. Gervasi, M. Zannoni and G. Sironi, CMB observations: improvements of the performance of correlation radiometers by signal modulation and synchronous detection, New Astron. 7 (2002) 125
- [23] M. Gervasi et al., Polarimetry in Astronomy, Proc. SPIE 4843 (2003) 336.
- [24] G.F. Smoot, C. Bennett, A. Kogut, E. Wright, J. Aymon et al., Structure in the COBE differential microwave radiometer first year maps, Astrophys. J. 396 (1992) L1
- [25] G. Sironi et al., A Search for Polarization of the Cosmic Microwave Background at 33 GHz Preliminary Observations of the South Celestial Pole Region, A.S.P. Conf. Ser. 141 (1998) 116.
- [26] M. Gervasi et al., Cosmic microwave polarization search: the Milano 33GHz polarimeter, SIF Conf. Proc. 68 (2000) 165
- [27] Planck collaboration, P. Ade et al., Planck 2013 results. XVI. Cosmological parameters, arXiv:1303.5076
- [28] A. Tartari, M. Zannoni, M. Gervasi, G. Boella and G. Sironi, TRIS. III. The Diffuse Galactic Radio Emission at $\hat{I}t'=+42\hat{a}\mathring{U}e$, Astrophys. J. 688 (2008) 32.
- [29] M. Zannoni et al., TRIS I: Absolute Measurements of the Sky Brightness Temperature at 0.6, 0.82 and 2.5 GHz, Astrophys. J. 688 (2008) 12, arXiv:0806.1415
- [30] M. Gervasi, A. Tartari, M. Zannoni, G. Boella and G. Sironi, The Contribution of the Unresolved Extragalactic Radio Sources to the Brightness Temperature of the Sky, Astrophys. J. 682 (2008) 223, arXiv:0803.4138
- [31] C. Ajello, G. Bonelli and G. Sironi, Evaluation of EarthâĂŹs atmospheric brightness temperature at decimetric wavelengths, Astrophys. J. Suppl. 96 (1995) 643.
- [32] S. Spinelli, G. Fabbian, A. Tartari, M. Zannoni and M.Gervasi, A template of atmospheric O2 circularly polarized emission for cosmic microwave background experiments, Mon. Not. Roy. Astron. Soc. 414 (2011) 3272, arXiv:1103.0160
- [33] J. Bond, A.H. Jaffe and L. Knox, Estimating the power spectrum of the cosmic microwave background, Phys. Rev. D 57 (1998) 2117, astro-ph/9708203
- [34] M. Tegmark, CMB mapping experiments: A DesignerâAZs guide, Phys. Rev. D 56 (1997) 4514, astro-ph/9705188.
- [35] M. Tegmark, An Icosahedron-Based Method for Pixelizing the Celestial Sphere, Astrophys. J. 470 (1996) L81 astro-ph/9610094
- [36] Planck collaboration, P. Ade et al., Planck 2013 results. XX. Cosmology from Sunyaev-Zeldovich cluster counts, arXiv:1303.5080